4D STEM with a direct electron detector

https://analyticalscience.wiley.com/do/10.1002/was.00010003

- Barnaby D.A. Levin, Chenyu Zhang, Benjamin Bammes, Paul M. Voyles, Robert B. Bilhorn

Overview

The recent development of fast, sensitive, pixelated detectors has led to the growing popularity of four-dimensional scanning transmission electron microscopy (4D STEM). 4D STEM involves acquiring a 2D convergent beam electron diffraction pattern, at every pixel of a 2D STEM raster, generating a 4D dataset containing a vast amount of information about the specimen. Here, we describe the basic principles of 4D STEM, including different types of information that can be extracted from 4D datasets and how the technique's dynamic range requirements can be met using a hybrid integrating and counting Monolithic Active Pixel Sensor (MAPS) Direct Detection Device (DDD®).

Introduction

Scanning transmission electron microscopy (STEM) is a powerful tool for studying specimens at very high (sub-angstrom) spatial resolution. Conventional detectors for STEM, such as bright-field (BF), annular bright-field (ABF), annular dark-field (ADF) and high angle annular dark-field (HAADF) detectors are monolithic, and form images, $I(x, y)$, by integrating the total signal over a range of scattering angles in the diffraction plane as the focused STEM probe is rastered over a two-dimensional (2D) area of a specimen (Figure 1a). In contrast, detectors for four-dimensional STEM (4D STEM) record a pixelated, angle-resolved 2D convergent beam electron diffraction (CBED) pattern, $I(k_x, k_y)$, for every position, (x, y), in the 2D STEM raster over the specimen (Figure 1b), yielding a 4D dataset, $I(k_x, k_y, x, y)$. As with any diffraction pattern in TEM, the angles in the diffraction plane sampled in 4D STEM may be controlled by varying the microscope camera length. The size of diffraction discs in the CBED pattern may be controlled by varying the convergence angle of the STEM probe. The choice of camera length and convergence angle will depend on the types of data that one wishes to extract from the 4D STEM dataset.

The key advantage of 4D STEM compared to conventional 2D STEM imaging is that, in a single scan, one can acquire a 4D dataset that contains all possible 2D STEM images of the sample, as well as a variety of novel signals that cannot be derived from conventional 2D STEM imaging. The speed and sensitivity of 4D data collection can be improved by employing a direct electron detector, which can either be used as a stand-alone detector or can be used alongside conventional STEM detectors. For example, a 4D STEM detector can work in conjunction with a traditional annular detector, which can record a 2D image using the signal from a region of the diffraction plane outside of that recorded by the 4D STEM detector. This flexibility allows users to upgrade their existing STEM instruments with 4D STEM capability.

Here, we give a basic overview of the principles of 4D STEM, including some of the types of images that can be extracted from 4D STEM datasets, as well as an overview of the types of direct detectors that can be used for 4D STEM. A complete review of the technique, including historical developments may be found in Ref. [1].

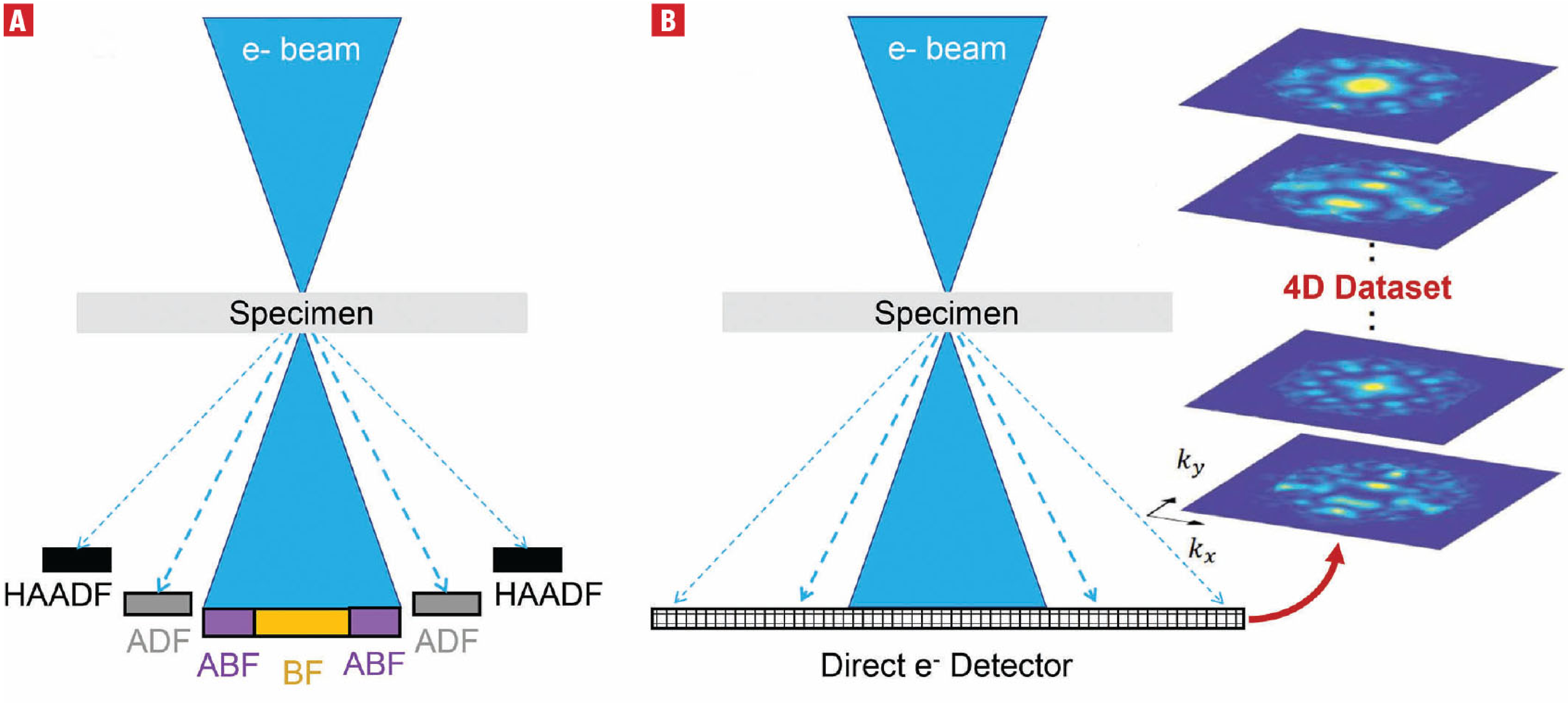

Figure 1. Schematic diagrams illustrating conventional STEM and 4D STEM. a) In conventional STEM, monolithic detectors are used to produce images by integrating a signal from different angular regions of the diffraction plane. b) In 4D STEM, an entire 2D CBED pattern is recorded at each probe position of a 2D STEM raster, resulting in a 4D dataset.

4D STEM Detectors

The availability of high-performance electron detectors has been one of the main catalysts for the growing popularity of 4D STEM[1]. Early efforts at recording 4D datasets consisting of CBED patterns were limited by the relatively slow readout speeds of CCDs[2-4,5]. Recording 4D STEM data is considerably more practical when using a sensitive detector capable of millisecond or sub-millisecond readout speeds. Although 4D STEM is possible using a fast scintillator coupled camera, direct electron detectors are particularly well-suited to 4D STEM due to their high detective quantum efficiency (DQE) and high signal to noise ratio (SNR) compared to scintillator coupled cameras.

There are two principal types of direct electron detector that have been used for 4D STEM applications, and both types have different strengths and weaknesses. A hybrid pixel array detector (PAD)[6, 7] consists of an array of wide, thick pixels (e.g. 150 x 150 x 500 µm for the electron microscope pixel array detector (EMPAD) described in Ref. [7] (Thermo Fisher Scientific, Waltham, MA USA) bump-bonded to an application specific integrated circuit. PADs typically exhibit extremely high dynamic range, due to a high saturation value per pixel[7], but their relatively small number of pixels limits the angular resolution of the detector and limits the ability to use the PAD as an "all-in-one" detector that can be used for other TEM imaging applications, where a large number of pixels is advantageous. In contrast, monolithic active pixel sensors (MAPS)[8-11] use relatively thin pixels, which limits beam spreading within each pixel, allowing for smaller pixel sizes (e.g. 6.5 x 6.5 µm in the case of a DE-16 (Direct Electron, San Diego, CA USA)) and a correspondingly much larger number of pixels per sensor. The traditional weakness of MAPS detectors for 4D STEM is their relatively limited dynamic range, due to a relatively low saturation value per pixel. This can be mitigated to some degree by using the large number of pixels on the sensor to spread features of interest in the CBED pattern over many pixels.

In many 4D-STEM experiments, it is desirable to simultaneously record very bright and faint features in the CBED pattern without saturating the detector. For example, one may wish to simultaneously record the bright central (0,0) beam (bright-field disc), as well as the faint signal of scattered electrons in the dark-field region. To maximize the signal-to-noise ratio of in the sparse dark-field region, MAPS detectors can be used to perform electron counting[12,13], which excludes background noise and normalizes the signal of each detected electron. However, isolating and counting each primary electron incident on the detector requires sparsity (i.e. < ~0.1 e^- per pixel), which is generally not satisfied in the intense bright-field disc. Hybrid counting and integrating techniques can provide a method of overcoming the challenge of limited dynamic range for 4D STEM using MAPS detectors[14,15].

Direct Electron has developed a patent-pending hybrid counting technique[15], which is implemented for our DE-16 detector. The workflow of the method is illustrated in Figure 2. During 4D STEM data acquisition, specialized software (DE-4DExplorer) is used to calculate a sparsity map for each frame. The sparsity map is a binary mask corresponding to regions of the frame where the number of primary electrons per pixel is low enough to be processed using electron counting. In these sparse regions (primarily in the dark-field area of the diffraction pattern), individual primary electron events can be distinguished and thus electron counting can be used to improve SNR by effectively eliminating the Landau noise caused by the variable amount of energy deposited on the sensor by each primary electron[16,17]. In bright regions (such as the bright-field disc), there is a sufficient number of primary electrons to statistically diminish Landau noise. However, in these bright areas many primary electrons are recorded by the same or neighbouring pixels, making it impossible to distinguish individual electron events using electron counting algorithms. To maximize the SNR without sacrificing linearity, the hybrid counting technique performs electron counting in the sparse regions of the CBED pattern while using conventional integration in non-sparse regions. The intensity of non-sparse regions is scaled based on the average pixel intensity per primary electron. Thus, the intensity value for each pixel in the final processed frame approximately corresponds to the actual number of primary electrons incident on each pixel in each frame. By applying this hybrid counting technique, the DE-16 can image the low-angle dark-field regions of the CBED pattern with a high SNR, while simultaneously recording useful information from the more intense bright-field disc.

Note that Direct Electron’s hybrid counting method automatically detects sparse regions in each recorded camera frame without prior information from the user. Electron counting is performed without manually having to define the position and size of the bright and sparse regions in advance. In principle, hybrid counting may therefore be applicable not only to 4D STEM, but also to other techniques that require high sensitivity and high dynamic range, such as electron energy loss spectroscopy (EELS).

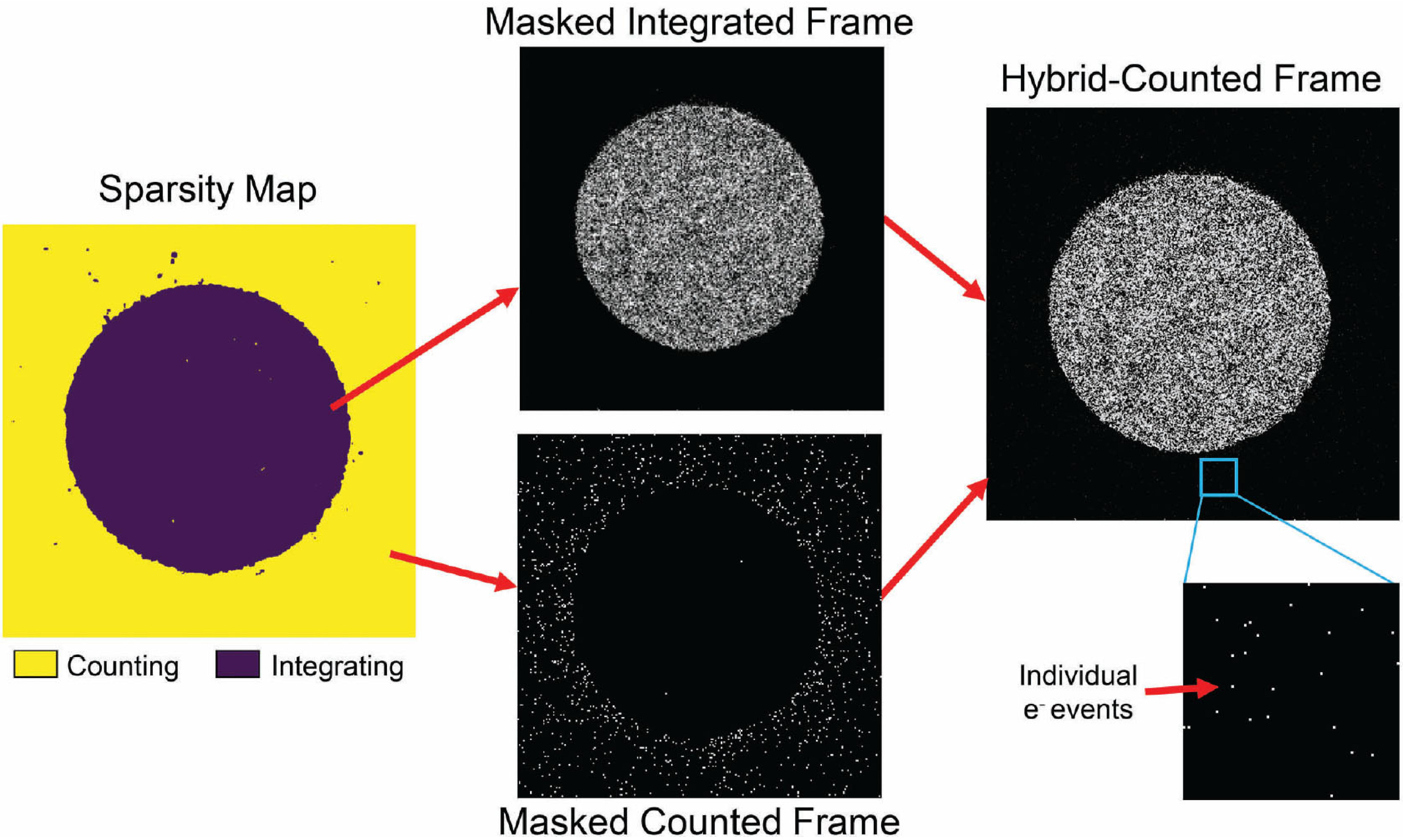

Figure 2. Illustration of the hybrid-counting technique. During data acquisition, the DE-4DExplorer software calculates a sparsity map for each frame. This is a binary mask corresponding to regions of the frame where the number of primary electrons per pixel is low enough to be processed by electron counting. Within the masked (yellow) area of the frame, data is recorded in counting mode. In the remaining area, data is collected in integrating mode. The data is then merged to form a hybrid counted frame, exhibiting a high SNR in the dark-field region, whilst simultaneously preserving information from the more intense bright-field disc.

4D STEM Data Analysis

4D STEM datasets occupy far more computer memory than a conventional STEM image. For example, a 4D STEM dataset consisting of a 1024x1024 pixel CBED pattern recorded at every pixel of a 1024x1024 STEM raster and stored in 16-bit format will occupy ~2 TB of memory. The acquisition of 4D STEM data also requires very high rates of data transfer compared to 2D STEM imaging. For example, a data transfer rate of ~2 GBs^{-1} is required for 4D STEM acquisition of 16-bit 1024x1024 pixel CBED patterns at a rate of one frame per millisecond. In practice, the memory occupied by a 4D STEM dataset may be reduced either by limiting the number of spatial pixels in the STEM raster, by using fewer pixels to record patterns in diffraction space, or by downsampling the data after acquisition.

Analysis of 4D STEM datasets typically requires a powerful computer and specialized software. The data presented below has been analyzed using a combination of custom written Python code, as well as libraries from Hyperspy[18] and py4DSTEM[19]. Other software tools currently available for the analysis of 4D STEM data include LiberTEM[20], Pycroscopy[21], pixStem[22], pyXem[23] and the Cornell Spectrum Imager plugin for ImageJ[24], which was originally written for the analysis of hyperspectral data, but now also includes 4D tools.

One of the simplest operations that can be applied to the 4D dataset is to mask an area of diffraction space and integrate the signal from within the mask in each diffraction pattern to recover a 2D STEM image[6,25,26]. This is illustrated in Figure 3 for a 4D dataset recorded from a sample of $SrTiO_3$ imaged along a [001] direction. Using this masking technique, images equivalent to that of any conventional STEM detector (e.g. BF, ABF, ADF) can be generated, but with the advantage that the 4D STEM dataset allows complete flexibility in choosing detector angles. Indeed, one can vary the shape and position of the mask, to generate images from any kind of “virtual detector”[27]. For example, one can choose to reduce the convergence angle of the STEM probe such that Bragg discs are well separated and do not overlap. In this mode, diffraction patterns are often referred to as nanobeam electron diffraction (NBED) or nanobeam diffraction (NBD) patterns, rather than CBED patterns. One can then generate an image analogous to that of dark-field TEM by placing a circular mask around a diffracted Bragg disc in the NBED pattern, with the mask acting as a virtual objective aperture[28-32].

In addition to reconstructing images using simple masks, 4D STEM enables the reconstruction of differential phase contrast (DPC) images[2,33-35], which were previously only available by using segmented detectors[36], and “Centre of Mass” (COM) images[6,37], which are unique to 4D STEM, and have also been referred to as “first moment” or COM DPC images in the literature[1,35,38]. DPC and COM both essentially measure the magnitude and direction of the average shift in the 2D momentum of the electron probe for each CBED pattern in the 4D STEM dataset. The DPC and COM imaging modes are sensitive to specimen and crystal grain orientation[6], as well as to electric fields in the specimen[33,39-44], which can cause a shift in the average momentum of the electron probe either by displacing the entire diffraction pattern, or altering the distribution of intensity within the diffraction pattern, depending on the relative length scales of the probe and the source of the field[37]. Magnetic fields can also be detected using DPC and COM when operating the microscope in a Lorentz mode[2,7,34,45,46]. An example of COM imaging is shown in Figure 4. For a diffraction pattern consisting of pixels with coordinates $k = (k_x, k_y)$, and with the intensity in each pixel defined as $I(k)$, the position of the centre of mass in the diffraction pattern can be defined mathematically as:

$$k_{COM}=\int k\, I(k)\, \mathrm{d}k$$

A suitable choice of origin for measuring k_{COM} is the position of the centre of the probe in vacuum when no specimen is present, which under ideal conditions should correspond to the centre of the optic axis and the centre of the detector. The effect of the nuclear potential on the COM is apparent when imaging a specimen at atomic resolution[33,39,47,48]. Figures 4a and 4b show the magnitude and direction respectively of the shift of the COM for the same area of the $SrTiO_3$ sample displayed in the images in Figure 3. The magnitude of the shift of the COM is strongest when the probe is close to, but not directly on top of, the Sr and Ti/O columns, and the direction of the shift is oriented towards the columns. Here, the COM images are measuring the deflection of the negatively charged electron beam by the screened, positively charged atomic nuclei.

As with the generation of conventional STEM images from 4D STEM data, one has complete flexibility to apply a mask of any shape or size to the 4D dataset when generating DPC or COM images, enabling the DPC or COM associated with specific regions of the CBED or NBED pattern to be calculated[37].

Another application of 4D STEM is mapping local changes in lattice constant and local strain within the specimen[49-51]. Strain information can be extracted from 4D STEM datasets in different ways. When acquiring 4D STEM data containing NBED patterns with well separated Bragg discs, strain is encoded in the disc positions[52], or (for very thin samples) the disc centre of mass[53]. For polycrystalline or amorphous materials, the ellipticity of NBED patterns may also be useful[54].

Further techniques that can make use of 4D STEM datasets include mapping of crystal grain orientations in a specimen[3,4,55-57], where there is some overlap between 4D STEM and the similar technique of nanobeam precession electron diffraction[58], and electron ptychography, in which computational methods are used to reconstruct the projected potential of the specimen, with the potential for spatial resolution beyond that of traditional STEM imaging techniques[59-70]. A number of other imaging modes besides those mentioned above may also be performed using 4D STEM[1]. As 4D STEM is a relatively new and growing technique, there may be further imaging modes that are yet to be developed that can take advantage of the wealth of information contained in 4D STEM datasets.

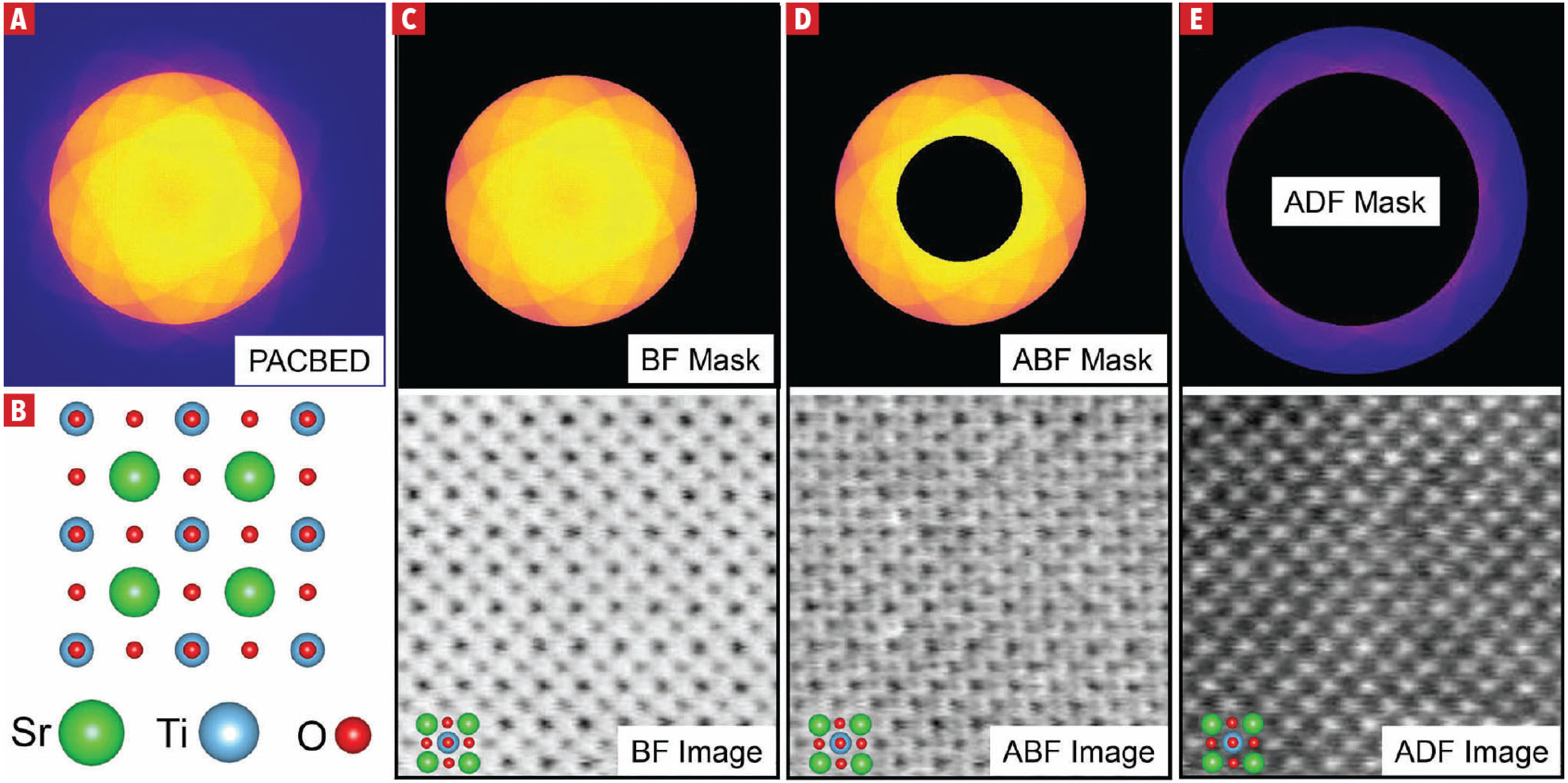

Figure 3. a) A position-averaged CBED (PACBED) pattern, derived from a 4D STEM dataset acquired from a SrTiO3 sample, imaged along a [001] direction. b) Diagram of the crystal structure of SrTiO3 in a [001] projection. c) Example of a mask that can be applied to the 4D dataset to produce a BF image. d) Example of a mask that can be applied to the 4D dataset to produce an ABF image. e) Example of a mask that can be applied to the 4D dataset to produce an ADF image. The crystal diagram in the lower corner of each image indicates atomic column positions. The spacing between adjacent Sr atomic columns (green) is ~3.9 Å.

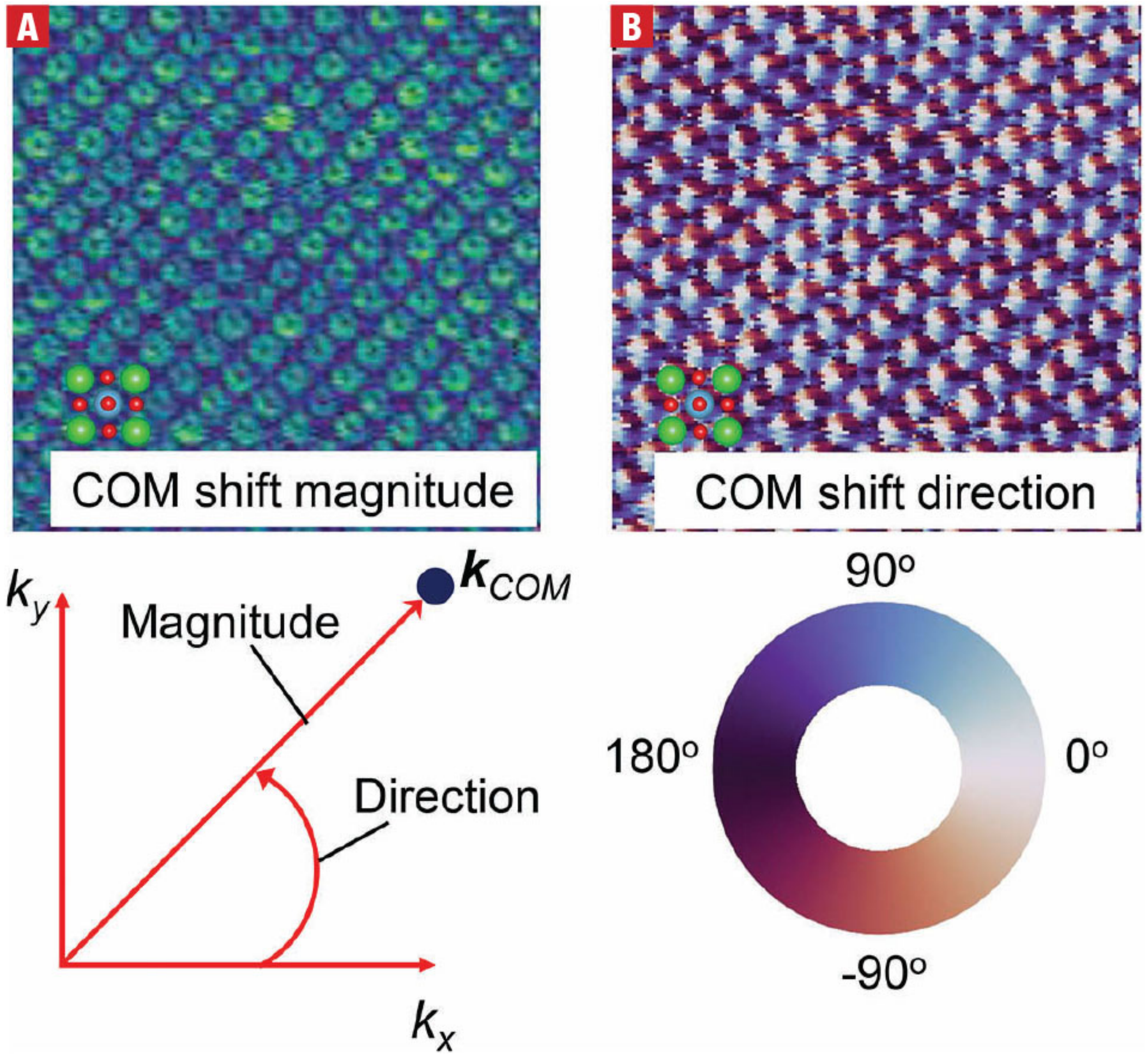

Figure 4. a) Image showing the magnitude of COM shifts in a 4D STEM dataset acquired from a sample of SrTiO3. The largest COM shifts occur when the probe is adjacent to an atomic column. The diagram be-neath the image illustrates how the magnitude and direction of the shift in the COM are defined with respect to the position of the centre of the probe in vacuum. b) Map showing the direction of COM shifts from the same dataset as in (a). When the probe is positioned adjacent to an atomic column, the COM shifts towards the column. The direction indicated by each colour is shown by the colour wheel beneath the image.

Materials and Methods

The data presented in this article was acquired on an Aberration Corrected FEI/Thermo Scientific Titan 80-200 S/TEM (Thermo Fisher Scientific, Waltham, MA USA), operated at 200 kV with a STEM probe current of ~20 pA and a probe convergence semi-angle of 24.5 mrad. A DE-16 direct detection camera (Direct Electron, San Diego, CA USA) was used to record 4D STEM data. Each of the CBED patterns in the 4D STEM data was captured using a 1024x1024 pixel centred area of the 4096x4096 pixel sensor. A hardware binning of 2 was applied to the CBED patterns, reducing them to 512x512 pixels in size, allowing the 4D STEM dataset to be recorded at a rate of ~1100 frames per second (fps). Higher frame rates (up to >4200 fps) are accessible by further reducing readout area.

The wedge-shaped single crystal $SrTiO_3$ [100] test specimen was prepared by multistep mechanical polishing at 1.6° tilt, followed by further thinning in a Fischione 1050 ion mill (E.A. Fischione Instruments, Inc., Export, PA, USA). The specimen was gently cleaned using an Ibss GV10x DS Asher cleaner (Ibss Group Inc., Burlingame, CA, USA) before being transferred into the TEM column.

Summary and conclusions

In summary, 4D STEM is a versatile technique that enables a multitude of different types of analyses to be performed on a specimen. These include reconstructing images equivalent to those of any traditional STEM detector of any shape or size, imaging of electric and magnetic fields, mapping strain within a specimen, mapping crystal grain orientations, analyzing medium range order, and generating ptychographic reconstructions with high spatial resolution. Both hybrid PADs and MAPS detectors may be used for 4D STEM. Using a hybrid counting method, implemented on detectors such as the DE-16, dynamic range and sensitivity are sufficient to allow simultaneous imaging of the bright-field disc and low-angle dark-field regions, overcoming a traditional weakness of the MAPS architecture, allowing users to record 4D STEM datasets that take advantage of the angular resolution available to a detector with a high pixel count. 4D STEM methods using pixelated direct electron detectors can complement existing STEM detectors and can readily be implemented on existing STEM instruments.

Acknowledgements

This material is based upon worksupported by U.S. D.O.E., Office of Science, Award Numbers DE-SC0018493 and DE-FG02- 08ER46547, and made use of UW-Madison microscopy facilities supported by Wisconsin MRSEC (DMR-1720415).

Author

Barnaby D.A. Levin,[1] Chenyu Zhang,[1] Benjamin Bammes,[1] Paul M. Voyles,[2] Robert B. Bilhorn[1]

Affiliation
1 Direct Electron LP, San Diego, CA, USA 2 Department of Materials Science And Engineering, University of Wisconsin Madison, Madison, WI, USA.

Contact
Barnaby D.A. Levin: blevin@directelectron.com

References

[1] Ophus, C. (2019). Four-dimensional scanning transmission electron microscopy (4D STEM): from scanning nanodiffraction to ptychography and beyond. *Microscopy and Microanalysis* 25, 563–582.

[2] Zaluzec, N. J. (2002). Quantitative measurements of magnetic vortices using position resolved diffraction in Lorentz STEM. *Microscopy and Microanalysis* 8, 376–377.

[3] Fundenberger, J.-J., Morawiec, A., Bouzy, E. & Lecomte, J. S. (2003). Polycrystal orientation maps from TEM. *Ultramicroscopy* 96, 127–137.

[4] Watanabe, M. & Williams, D. (2007). Development of diffraction imaging for orientation analysis of grains in scanning transmission electron microscopy. *Microscopy and Microanalysis* 13 (S02), 962-963.

[5] Voyles, P. M. & Muller, D. A. (2002). Fluctuation microscopy in the STEM. *Ultramicroscopy* 93, 147–159.

[6] Caswell, T. A., Ercius, P., Tate, M. W., Ercan, A., Gruner, S. M. & Muller, D. A. (2009). A high-speed area detector for novel imaging techniques in a scanning transmission electron microscope. *Ultramicroscopy* 109, 304–311.

[7] Tate, M. W., Purohit, P., Chamberlain, D., Nguyen, K. X., Hovden, R., Chang, C. S., Deb, P., Turgut, E., Heron, J. T., Schlom, D. G., Ralph, D. C., Fuchs, G. D., Shanks, K. S., Philipp, H. T., Muller, D. A. & Gruner, S. M. (2016). High dynamic range pixel array detector for scanning transmission electron microscopy. *Microscopy and Microanalysis* 22, 237–249.

[8] Xuong, N.-H., Milazzo, A.-C., LeBlanc, P., Duttweiler, F., Bouwer, J., Peltier, S., Ellisman, M., Denes, P., Bieser, F., Matis, H. S., Wieman, H. & Kleinfelder, S. (2004). First use of a high-sensitivity active pixel sensor array as a detector for electron microscopy. *Proc. SPIE.* 5301, Sensors and Camera Systems for Scientific, Industrial, and Digital Photography Applications V.

[9] Milazzo, A.-C., Leblanc, P., Duttweiler, F., Jin, L., Bouwer, J. C., Peltier, S., Ellisman, M., Bieser, F., Matis, H. S., Wieman, H., Denes, P., Kleinfelder, S. & Xuong, N.-H. (2005). Active pixel sensor array as a detector for electron microscopy. *Ultramicroscopy* 104, 152–159.

[10] Faruqi, A. R., Henderson, R., Pryddetch, M., Allport, P. & Evans, A. (2005). Direct single electron detection with a CMOS detector for electron microscopy. *Nuclear Instruments and Methods in Physics Research Section A: Accelerators, Spectrometers, Detectors and Associated Equipment* 546, 170–175.

[11] Deptuch, G., Besson, A., Rehak, P., Szelezniak, M., Wall, J., Winter, M. & Zhu, Y. (2007). Direct electron imaging in electron microscopy with monolithic active pixel sensors. *Ultramicroscopy* 107, 674–684.

[12] Jin L. (2009). Direct electron detection in transmission electron microscopy. University of California, San Diego: San Diego, CA.

[13] McMullan, G., Clark, A. T., Turchetta, R. & Faruqi, A. R. (2009). Enhanced imaging in low dose electron microscopy using electron counting. *Ultramicroscopy* 109, 1411–1416.

[14] Gallagher-Jones, M., Ophus, C., Bustillo, K. C., Boyer, D. R., Panova, O., Glynn, C., Zee, C.-T., Ciston, J., Mancia, K. C., Minor, A. M. & Rodriguez, J. A. (2019). Nanoscale mosaicity revealed in peptide microcrystals by scanning electron nanodiffraction. *Communications Biology* 2, 26.

[15] Bammes, B., Ramachandra, R., Mackey, M. R., Bilhorn, R. & Ellisman, M. (2019). Multi-color electron microscopy of cellular ultrastructure using 4D STEM. *Microscopy and Microanalysis* 25, 1060–1061.

[16] Landau, L. (1944). On the energy loss of fast particles by ionization. *Journal of Physics USSR* 8, 201-205.

[17] McMullan, G., Faruqi, A. R., Clare, D. & Henderson, R. (2014). Comparison of optimal performance at 300keV of three direct electron detectors for use in low dose electron microscopy. *Ultramicroscopy* 147, 156–163.

[18] de la Peña, F., Prestat, E., Fauske, V.T., Burdet, P., Jokubauskas, P. Nord, M. … Garmannslund, A., (2019). hyperspy/hyperspy: HyperSpy v1.5.2 (Version v1.5.2). Zenodo. http://doi.org/10.5281/zenodo.3396791 (Accessed December 18, 2019).

[19] Savitzky, B. H., Hughes, L., Bustillo, K. C., Deng, H. D., Jin, N. L., Lomeli, E. G., Chueh, W. C., Herring, P., Minor, A. & Ophus, C. (2019). py4DSTEM: open source software for 4D STEM data analysis. *Microscopy and Microanalysis* 25, 124–125.

[20] Clausen, A., Weber, D., Ruzaeva, K., Migunov, V., Caron, J., Chandra, R., … Dunin-Borkowski, R.. (2019). LiberTEM/LiberTEM: 0.3.0 (Version 0.3.0). Zenodo. http://doi.org/10.5281/zenodo.3572855 (Accessed December 18, 2019).

[21] Somnath, S., Smith, C. R., Laanait, N., Vasudevan, R. K., Ievlev, A., Belianinov, A., Lupini, A. R., Shankar, M., Kalinin, S. V., and Jesse, S., (2019). USID and Pycroscopy – Open frameworks for storing and analyzing spectroscopic and imaging data. arXiv: 1903.09515.

[22] Nord, M., Webster, R. W. H., Paton, K. A., McVitie, S., McGrouther, D., MacLaren, I. & Paterson, G. W. (2019). Fast pixelated detectors in scanning transmission electron microscopy. Part I: Data Acquisition, Live Processing and Storage. *arXiv:1911.11560 [cond-mat, physics:physics]*. http://arxiv.org/abs/1911.11560 (Accessed December 18, 2019).

[23] Johnstone, D.N., Crout, P., Laulainen, J., Høgås, S., Martineau, B., Bergh, T., … Tovey, R., (2019, November 9). pyxem/pyxem: pyxem 0.10.0 (Version v0.10.0). Zenodo. http://doi.org/10.5281/zenodo.3533653 (Accessed December 18, 2019).

[24] Hovden, R., Cueva, P., Mundy, J. A. & Muller, D. A. (2013). The open-source Cornell Spectrum Imager. *Microscopy Today* 21, 40–44.

[25] Kimoto, K. & Ishizuka, K. (2011). Spatially resolved diffractometry with atomic-column resolution. *Ultramicroscopy* 111, 1111–1116.

[26] Gammer, C., Burak Ozdol, V., Liebscher, C. H. & Minor, A. M. (2015). Diffraction contrast imaging using virtual apertures. *Ultramicroscopy* 155, 1–10.

[27] Jones, L. & Nellist, P. D. (2013). Advances in 2D, 3D and 4D STEM image data analysis. *Microscopy and Microanalysis* 19, 770–771.

[28] Schaffer, B., Gspan, C., Grogger, W., Kothleitner, G. & Hofer, F. (2008). Hyperspectral imaging in TEM: new ways of information extraction and display. *Microscopy and Microanalysis* 14, 70–71.

[29] Tao, J., Niebieskikwiat, D., Varela, M., Luo, W., Schofield, M. A., Zhu, Y., Salamon, M. B., Zuo, J. M., Pantelides, S. T. & Pennycook, S. J. (2009). Direct imaging of nanoscale phase separation in La 0.55 Ca 0.45 MnO_3: relationship to colossal magnetoresistance. *Physical Review Letters* 103, 097202.

[30] Im, S., Chen, Z., Johnson, J. M., Zhao, P., Yoo, G. H., Park, E. S., Wang, Y., Muller, D. A. & Hwang, J. (2018). Direct determination of structural heterogeneity in metallic glasses using four-dimensional scanning transmission electron microscopy. *Ultramicroscopy* 195, 189–193.

[31] Shukla, A. K., Ramasse, Q. M., Ophus, C., Kepaptsoglou, D. M., Hage, F. S., Gammer, C., Bowling, C., Gallegos, P. A. H. & Venkatachalam, S. (2018). Effect of composition on the structure of lithium- and manganese-rich transition metal oxides. *Energy & Environmental Science* 11, 830–840.

[32] Levin, B. D. A., Finnefrock, A. C., Hull, A. M., Thomas, M. G., Holtz, M. E., Plahter, U., Grimstad, I., Mass, J. L. & Muller D.M. (2019). Revealing the nanoparticle composition of Edvard Munch's The Scream, and implications for paint alteration in iconic early 20th century artworks. arXiv:1909.01933 [cond-mat.mtrl-sci].

[33] Müller, K., Krause, F. F., Béché, A., Schowalter, M., Galioit, V., Löffler, S., Verbeeck, J., Zweck, J., Schattschneider, P. & Rosenauer, A. (2014). Atomic electric fields revealed by a quantum mechanical approach to electron picodiffraction. *Nature Communications* 5, 5653.

[34] Krajnak, M., McGrouther, D., Maneuski, D., Shea, V. O. & McVitie, S. (2016). Pixelated detectors and improved efficiency for magnetic imaging in STEM differential phase contrast. *Ultramicroscopy* 165, 42–50.

[35] Chen, Z., Weyland, M., Ercius, P., Ciston, J., Zheng, C., Fuhrer, M. S., D'Alfonso, A. J., Allen, L. J. & Findlay, S. D. (2016). Practical aspects of diffractive imaging using an atomic-scale coherent electron probe. *Ultramicroscopy* 169, 107–121.

[36] Haider, M., Epstein, A., Jarron, P. & Boulin, C. (1994). A versatile, software configurable multichannel STEM detector for angle-resolved imaging. *Ultramicroscopy* 54, 41–59.

[37] Cao, M. C., Han, Y., Chen, Z., Jiang, Y., Nguyen, K. X., Turgut, E., Fuchs, G. D. & Muller, D. A. (2018). Theory and practice of electron diffraction from single atoms and extended objects using an EMPAD. *Microscopy* 67, i150–i161.

[38] Müller-Caspary, K., Krause, F. F., Winkler, F., Béché, A., Verbeeck, J., Van Aert, S. & Rosenauer, A. (2019). Comparison of first moment STEM with conventional differential phase contrast and the dependence on electron dose. *Ultramicroscopy* 203, 95–104.

[39] Hachtel, J. A., Idrobo, J. C. & Chi, M. (2018). Sub-Ångstrom electric field measurements on a universal detector in a scanning transmission electron microscope. *Advanced Structural and Chemical Imaging* 4, 10.

[40] Das, S., Tang, Y. L., Hong, Z., Gonçalves, M. A. P., McCarter, M. R., Klewe, C., Nguyen, K. X., Gómez-Ortiz, F., Shafer, P., Arenholz, E., Stoica, V. A., Hsu, S.-L., Wang, B., Ophus, C., Liu, J. F., Nelson, C. T., Saremi, S., Prasad, B., Mei, A. B., Schlom, D. G., Íñiguez, J., García-Fernández, P., Muller, D. A., Chen, L. Q., Junquera, J., Martin, L. W. & Ramesh, R. (2019). Observation of room-temperature polar skyrmions. *Nature* 568, 368–372.

[41] Fang, S., Wen, Y., Allen, C. S., Ophus, C., Han, G. G. D., Kirkland, A. I., Kaxiras, E. & Warner, J. H. (2019). Atomic electrostatic maps of 1D channels in 2D semiconductors using 4D scanning transmission electron microscopy. *Nature Communications* 10, 1127.

[42] Gao, W., Addiego, C., Wang, H., Yan, X., Hou, Y., Ji, D., Heikes, C., Zhang, Y., Li, L., Huyan, H., Blum, T., Aoki, T., Nie, Y., Schlom, D. G., Wu, R. & Pan, X. (2019). Real-space charge-density imaging with sub-Ångström resolution by four-dimensional electron microscopy. *Nature* 575, 480–484.

[43] Müller-Caspary, K., Grieb, T., Müßener, J., Gauquelin, N., Hille, P., Schörmann, J., Verbeeck, J., Van Aert, S., Eickhoff, M. & Rosenauer, A. (2019). Electrical polarization in AlN/GaN nanodisks measured by momentum-eesolved 4D scanning transmission electron microscopy. *Physical Review Letters* 122, 106102.

[44] Yadav, A. K., Nguyen, K. X., Hong, Z., García-Fernández, P., Aguado-Puente, P., Nelson, C. T., Das, S., Prasad, B., Kwon, D., Cheema, S., Khan, A. I., Hu, C., Íñiguez, J., Junquera, J., Chen, L.-Q., Muller, D. A., Ramesh, R. & Salahuddin, S. (2019). Spatially resolved steady-state negative capacitance. *Nature* 565, 468–471.

[45] Almeida, T.P., Temple, R., Massey, J. *et al.* Quantitative TEM imaging of the magnetostructural and phase transitions in FeRh thin film systems. *Sci Rep* 7, 17835 (2017)

[46] Nord, M., Semisalova, A., Kákay, A., Hlawacek, G., MacLaren, I., Liersch, V., Volkov, O. M., Makarov, D., Paterson, G. W., Potzger, K., Lindner, J., Fassbender, J., McGrouther, D. & Bali, R. (2019). Strain anisotropy and magnetic domains in embedded nanomagnets. *Small* 1904738.

[47] Müller-Caspary, K., Duchamp, M., Rösner, M., Migunov, V., Winkler, F., Yang, H., Huth, M., Ritz, R., Simson, M., Ihle, S., Soltau, H., Wehling, T., Dunin-Borkowski, R. E., Van Aert, S. & Rosenauer, A. (2018). Atomic-scale quantification of charge densities in two-dimensional materials. *Physical Review B* 98, 121408.

[48] Addiego, C., Gao, W. & Pan, X. (2020). Thickness and defocus dependence of inter-atomic electric fields measured by scanning diffraction. *Ultramicroscopy* 208, 112850.

[49] Ozdol, V. B., Gammer, C., Jin, X. G., Ercius, P., Ophus, C., Ciston, J. & Minor, A. M. (2015). Strain mapping at nanometer resolution using advanced nano-beam electron diffraction. *Applied Physics Letters* 106, 253107.

[50] Pekin, T. C., Ding, J., Gammer, C., Ozdol, B., Ophus, C., Asta, M., Ritchie, R. O. & Minor, A. M. (2019). Direct measurement of nanostructural change during in situ deformation of a bulk metallic glass. *Nature Communications* 10, 2445.

[51] Yu, Z., Zhang, C., Voyles, P. M., He, L., Liu, X., Nygren, K. & Couet, A. (2019). Microstructure and microchemistry study of irradiation-induced precipitates in proton irradiated ZrNb alloys. *Acta Materialia* 178, 228–240.

[52] Pekin, T. C., Gammer, C., Ciston, J., Minor, A. M. & Ophus, C. (2017). Optimizing disk registration algorithms for nanobeam electron diffraction strain mapping. *Ultramicroscopy* 176, 170–176.

[53] Han, Y., Nguyen, K., Cao, M., Cueva, P., Xie, S., Tate, M. W., Purohit, P., Gruner, S. M., Park, J. & Muller, D. A. (2018). Strain mapping of two-dimensional heterostructures with subpicometer precision. *Nano Letters* 18, 3746–3751.

[54] Gammer, C., Ophus, C., Pekin, T. C., Eckert, J. & Minor, A. M. (2018). Local nanoscale strain mapping of a metallic glass during *in situ* testing. *Applied Physics Letters* 112, 171905.

[55] Panova, O., Chen, X. C., Bustillo, K. C., Ophus, C., Bhatt, M. P., Balsara, N. & Minor, A. M. (2016). Orientation mapping of semicrystalline polymers using scanning electron nanobeam diffraction. *Micron* 88, 30–36.

[56] Panova, O., Ophus, C., Takacs, C. J., Bustillo, K. C., Balhorn, L., Salleo, A., Balsara, N. & Minor, A. M. (2019). Diffraction imaging of nanocrystalline structures in organic semiconductor molecular thin films. *Nature Materials* 18, 860–865.

[57] Ren, D., Padgett, E., Yang, Y., Shen, L., Shen, Y., Levin, B. D. A., Yu, Y., DiSalvo, F. J., Muller, D. A. & Abruña, H. D. (2019). Ultrahigh rate performance of a robust Lithium Nickel Manganese Cobalt oxide cathode with preferentially orientated Li-diffusing channels. *ACS Applied Materials & Interfaces* 11, 41178–41187.

[58] Rouviere, J.-L., Béché, A., Martin, Y., Denneulin, T. & Cooper, D. (2013). Improved strain precision with high spatial resolution using nanobeam precession electron diffraction. *Applied Physics Letters* 103, 241913.

[59] Nellist, P. D., McCallum, B. C. & Rodenburg, J. M. (1995a). Resolution beyond the 'information limit' in transmission electron microscopy. *Nature* 374, 630–632.

[60] Pennycook, T. J., Lupini, A. R., Yang, H., Murfitt, M. F., Jones, L. & Nellist, P. D. (2015). Efficient phase contrast imaging in STEM using a pixelated detector. Part 1: Experimental demonstration at atomic resolution. *Ultramicroscopy* 151, 160–167.

[61] Lupini, A. R., Chi, M., Kalinin, S. V., Borisevich, A. Y., Carlos Idrobo, J. & Jesse, S. (2015). Ptychographic imaging in an aberration corrected STEM. *Microscopy and Microanalysis* 21, 1219–1220.

[62] Yang, H., Jones, L., Ryll, H., Simson, M., Soltau, H., Kondo, Y., Sagawa, R., Banba, H., MacLaren, I. & Nellist, P. D. (2015). 4D STEM: High efficiency phase contrast imaging using a fast pixelated detector. *Journal of Physics: Conference Series* 644, 012032.

[63] Yang, H., Ercius, P., Nellist, P. D. & Ophus, C. (2016). Enhanced phase contrast transfer using ptychography combined with a pre-specimen phase plate in a scanning transmission electron microscope. *Ultramicroscopy* 171, 117–125.

[64] Yang, H., Rutte, R. N., Jones, L., Simson, M., Sagawa, R., Ryll, H., Huth, M., Pennycook, T. J., Green, M. L. H., Soltau, H., Kondo, Y., Davis, B. G. & Nellist, P. D. (2016). Simultaneous atomic-resolution electron ptychography and Z-contrast imaging of light and heavy elements in complex nanostructures. *Nature Communications* 7, 12532.

[65] Yang, H., MacLaren, I., Jones, L., Martinez, G. T., Simson, M., Huth, M., Ryll, H., Soltau, H., Sagawa, R., Kondo, Y., Ophus, C., Ercius, P., Jin, L., Kovács, A. & Nellist, P. D. (2017). Electron ptychographic phase imaging of light elements in crystalline materials using Wigner distribution deconvolution. *Ultramicroscopy* 180, 173–179.

[66] Wang, P., Zhang, F., Gao, S., Zhang, M. & Kirkland, A. I. (2017). Electron ptychographic diffractive imaging of Boron atoms in LaB6 crystals. *Scientific Reports* 7, 2857.

[67] dos Reis, R., Yang, H., Ophus, C., Ercius, P., Bizarri, G., Perrodin, D., Shalapska, T., Bourret, E., Ciston, J. & Dahmen, U. (2018). Determination of the structural phase and octahedral rotation angle in halide perovskites. *Applied Physics Letters* 112, 071901.

[68] Lozano, J. G., Martinez, G. T., Jin, L., Nellist, P. D. & Bruce, P. G. (2018). Low-dose aberration-free imaging of Li-rich cathode materials at various states of charge using electron ptychography. *Nano Letters* 18, 6850–6855.

[69] Jiang, Y., Chen, Z., Han, Y., Deb, P., Gao, H., Xie, S., Purohit, P., Tate, M. W., Park, J., Gruner, S. M., Elser, V. & Muller, D. A. (2018). Electron ptychography of 2D materials to deep sub-ångström resolution. *Nature* 559, 343–349.

[70] Wen, Y., Ophus, C., Allen, C. S., Fang, S., Chen, J., Kaxiras, E., Kirkland, A. I. & Warner, J. H. (2019). Simultaneous identification of low and high atomic number atoms in monolayer 2D materials using 4D scanning transmission electron microscopy. *Nano Letters* 19, 6482–6491.